

Beam Position Reconstruction for the g2p Experiment in Hall A at Jefferson Lab

Pengjia Zhu^{a,*}, Kalyan Allada^{b,g}, Trent Allison^b, Toby Badman^c, Alexandre Camsonne^b, Jian-ping Chen^b, Melissa Cummings^d, Chao Gu^e, Min Huang^f, Jie Liu^e, John Musson^b, Karl Slifer^c, Vincent Sulkosky^{e,g}, Yunxiu Ye^a, Jixie Zhang^{b,e}, Ryan Zielinski^c

^aUniversity of Science and Technology of China, Hefei, Anhui 230026, China

^bThomas Jefferson National Accelerator Facility, Newport News, VA 23606, USA

^cUniversity of New Hampshire, Durham, NH 03824, USA

^dCollege of William & Mary, Williamsburg, VA 23187, USA

^eUniversity of Virginia, Charlottesville, VA 22904, USA

^fDuke University, Durham, NC 27708, USA

^gMassachusetts Institute of Technology, MA, 02139, USA

Abstract

Beam-line equipment was upgraded for experiment E08-027 (g2p) in Hall A at Jefferson Lab. Two beam position monitors (BPMs) were necessary to measure the beam position and angle at the target. A new BPM receiver was designed and built to handle the low beam currents (50-100 nA) used for this experiment. Two new super-harps were installed for calibrating the BPMs. In addition to the existing fast raster system, a slow raster system was installed. Before and during the experiment, these new devices were tested and debugged, and their performance was also evaluated. In order to achieve the required accuracy (1-2 mm in position and 1-2 mrad in angle at the target location), new methods were developed for analyzing the data of the BPMs and harps, as well as reconstructing the beam position and angle event by event at the target location. The calculated beam position will be used in the data analysis to accurately determine the kinematics for each event.

Keywords: g2p; BPM; raster; beam position

*Corresponding author

Email address: pzhu@jlab.org, zhupj55@mail.ustc.edu.cn (Pengjia Zhu)

1. Introduction

A polarized ammonia (NH_3) target was used for the first time in Hall A for the g2p experiment [1]. It operated at a low temperature of 1K and a strong transverse magnetic field of either 5 T or 2.5 T. A high electron beam current would cause significant target polarization drop due to target temperature rising and ionization radiation to the target material [2]. To minimize depolarization, the beam current was limited to below 100 nA and a raster system was used to spread the beam spot out to a larger area. The transverse magnetic field in the target region would cause the beam to be deflected downward when the beam enters the target region. To compensate for this, two chicane magnets were placed in front of the target to pre-bend the beam upwards. Due to the low beam current and tight space limitations after the chicane magnets, the experimental accuracy goals for the position (1-2 mm) and angle (1-2 mrad) at the target were challenging to achieve. New beam-line devices and an associated readout electronics system were designed for the g2p experiment to accomplish these goals. Design details and the performance of the beam-line devices will be described in the following sections along with a discussion of a new analysis method determine the beam position and direction.

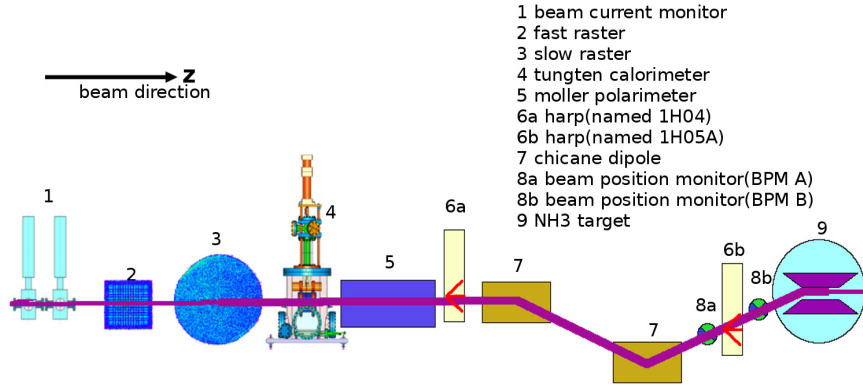


Figure 1: Schematic of beamline components for g2p experiment

2. Beam-line Instrumentation

2.1. Beam position monitor (BPM)

The scattering angle of the outgoing lepton in deep inelastic scattering, which is defined with respect to the direction of the incident beam, is an important variable for obtaining meaningful physics results. Therefore, the position and direction of the beam, after being bent by the chicane magnetic field and spread out by the rasters, must be measured precisely. Two BPMs and two harps were installed for relative and absolute measurements of beam position and direction near the target, respectively.

The BPM consists of four open-ended antennas for detecting the beam position; the measurement is non-invasive to the beam. The BPM chambers shown in Fig.2 and Fig. 3 are part of the beam pipe. The four antennas, x_+ , x_- , y_+ , y_- are attached to feedthroughs on the interior wall of the pipe at 90° intervals.

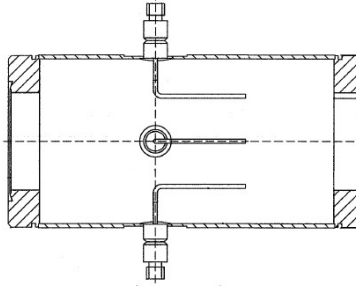


Figure 2: BPM chamber design diagram from JLab instrumentation group

When the beam passes through the BPM chamber, each antenna receives an induced signal. As shown in Fig. 3, the BPM receiver collects and sends the signal to the regular Hall A DAQ system and another DAQ system designed for parity violation experiments, the HAPPEX system [3]. The new BPM receiver was designed by the JLab instrumentation group [4] in order to achieve the required precision at a level of 0.1 mm with a beam current as low as 50 nA. The regular DAQ system was connected to a 13-bit fastbus ADC (Lecroy ADC

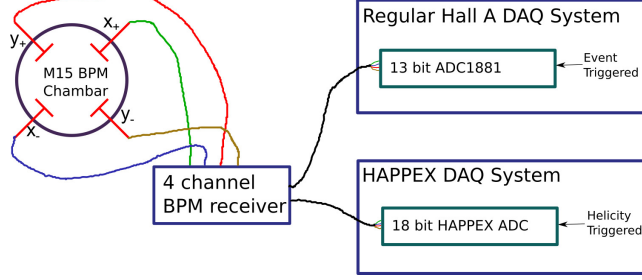


Figure 3: BPM chamber, receiver and related DAQ system for g2p experiment

1881) with an integration time of 50 ns, which was triggered by a scattered
 electron event. The HAPPEX system was connected to an 18-bit ADC with an
 integration time of 875 μ s, which was triggered by a beam helicity signal at 1
 kHz. The amplitude, A , recorded in the ADC has the following relation with
 the BPM signal, ϕ :

$$A \propto \phi \cdot 10^{g/20}, \quad (1)$$

where g is the gain of the receiver.

The BPM receiver generates a large time delay for the output signals. The digital filter used in the receiver contributes 1/175 s delay time, which was the inverse of the bandwidth setting chosen for the filter. There is a $\sim 4 \mu$ s delay as a result of finite processing times. The BPM can not provide event by event position because of this time delay, due to the high frequency fast raster system (discussed in chapter 2.3).

The existed chicane dipole magnets ordained two BPMs must be installed after them. Because of the space limitation between the second chicane magnet and the target, the two BPMs were placed very close to each other. One was placed 95.5 cm upstream of the target while the other was placed 69 cm upstream, making the distance between them only 26.5 cm. The short distance magnified the position uncertainty from the BPMs to target.

73 *2.2. Super harp*

74 Two super harps were designed and installed in the beam-line, as shown in
 75 Fig.1 (label 6a - 1H04 and 6b - 1H05A), to provide an absolute measurement
 76 of the beam position for calibration of the BPMs. The new harps were able to
 77 work in pulsed beam (1% duty factor) with a current of several μA . A diagram
 for the harp is shown in Fig.4,

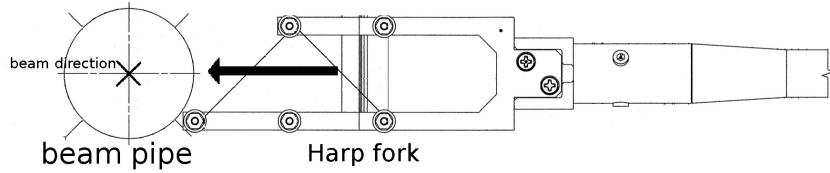


Figure 4: Harp diagram

78

79 which consists of three wires with a thickness of $50\ \mu\text{m}$, a fork and a controller
 80 chassis. The harp chamber is perpendicular to the beam pipe and connected
 81 to the beam pipe as part of the vacuum chamber of the beamline. The two
 82 harps have different configurations of three wires: vertical(|), bank left(\), and
 83 bank right(/) for 1H04, and /, |, \ for 1H05. The angle of the / or \ wires is
 84 45° relative to the wire dock frame. The wires are arranged in a fork (Fig.4)
 85 controlled by a step motor [5] which can be moved in and out of the beam-line.
 86 The harps must be moved out of the beam-line when production data is being
 87 taken because they are invasive to the beam. The original position of the wires
 88 was surveyed before the experiment at a precision level of 0.1 mm. As the motor
 89 driver moved the fork through the beam, each wire received a signal, which was
 90 recorded for further analysis. The signals received from the wire and the step-
 91 counters from the motor driver were then sent to an amplifier and the DAQ.
 92 The amplification and the speed of the motor were adjustable for the purpose
 93 of optimizing the signals of each scan. Recorded data combined with the survey
 94 data was used to calculate the absolute beam position.

95 The signal from the | wire (*peak*) was used for getting the x position (x_{harp})

96 of the beam , and the signals from the /, \ wires ($peak_{/}$ and $peak_{\backslash}$) were used
 97 for getting the y position (y_{harp}):

$$\begin{aligned} x_{harp} &= survey_{|} - peak_{|} \\ y_{harp} &= \frac{1}{2}[(survey_{\backslash} - survey_{/}) - (peak_{\backslash} - peak_{/})] \end{aligned} \quad (2)$$

98 2.3. Raster system

99 In order to minimize the depolarization, avoid damage to the target material
 100 from radiation, and reduce systematic error for the polarization measurement
 101 by NMR (The polarization of the NH_3 target was measured by a NMR coil
 102 which installed inside the target cell [6]. The non-uniformity of depolarization
 103 could reduce the precision of the NMR measurement due to the measurement
 104 being an average over the target), two raster systems were installed at ~ 17 m
 105 upstream of the target, as shown in Fig.1 (labels 2 and 3 for fast and slow rasters,
 106 respectively). Both the fast and slow rasters consist of two dipole magnets. The
 107 same triangular waveforms with frequency of 25 kHz were used to drive the
 108 magnet coils of the fast raster to move the beam in x and y directions, forming
 a rectangular pattern of 2 mm \times 2 mm, as shown in Fig.5.

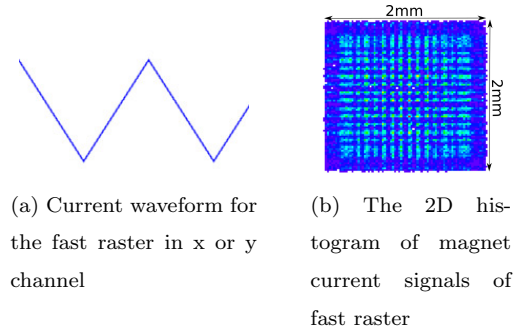


Figure 5: Fast raster pattern

109
 110 A dual-channel function-generator¹ was used to generate two independent

¹agilent 33522A function generator, <http://www.home.agilent.com/en/pd-1871286-pn-33522A/function-arbitrary-waveform-generator-30-mhz>

waveforms to drive the magnet coils of the slow raster. The waveforms for the

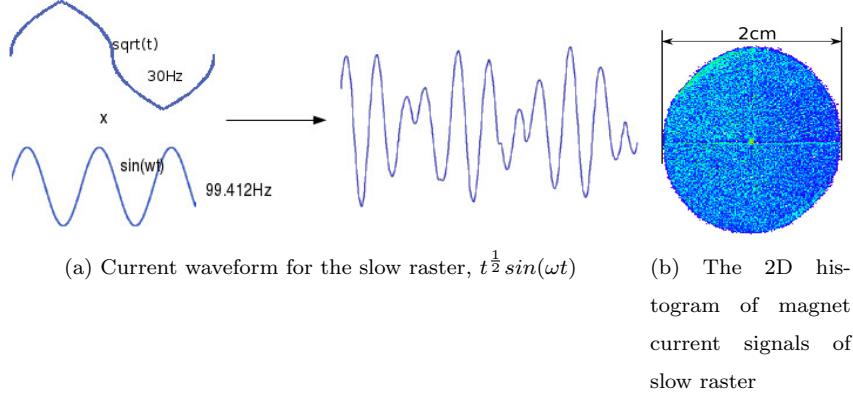


Figure 6: Slow raster pattern

111

112 x and y directions are:

$$\begin{aligned} x &= A_x(t + \text{amphase}_x)^{1/2} \sin(\omega_x t + \text{phase}_x), \\ y &= A_y(t + \text{amphase}_y)^{1/2} \sin(\omega_y t + \text{phase}_y), \end{aligned} \quad (3)$$

113 where the A_x and A_y are the maximum amplitude, the unit of $\text{amphase}_{x,y}$ is the
 114 same as t . Both of them are sine functions modulated by a function $t^{1/2}$ in order
 115 to generate a uniform circular pattern [7], as shown in Fig.6. The frequency of
 116 the x and y waveforms kept same: $\omega_x = \omega_y = 99.412$ Hz. In order to cycle the
 117 amplitude modulation (AM) function, four piece-wise functions are combined
 118 together. The first term is $t^{1/2}$, and the second term is $\text{period}/2 - t^{1/2}$, and so
 119 on for the third and fourth terms. The cycled function has the frequency of 30
 120 Hz.

121 Both sine and AM functions have a phase difference between the x and y
 122 waveform. The former could be locked by the function generator, the latter
 123 could not be locked and caused a non-uniformity pattern, as shown in Fig.7(a).
 124 A simulation was done to reproduce the non-uniformity by setting the phase
 125 difference to non-zero, as shown in Fig.7(b). The phase difference in the AM
 126 function was carefully adjusted and minimized before production data taking

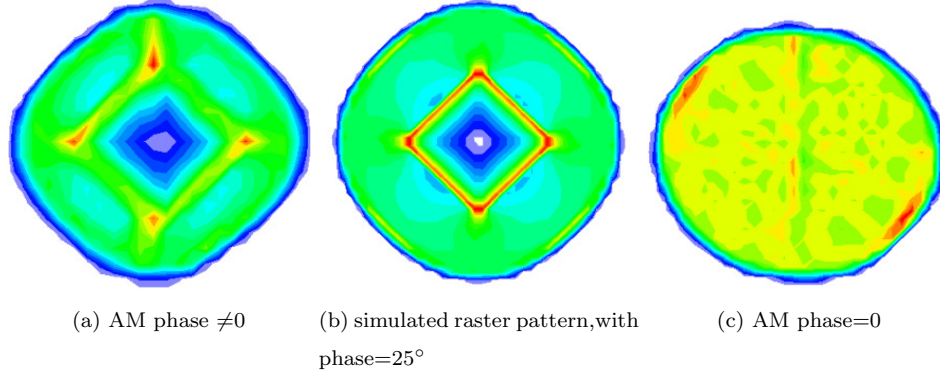


Figure 7: Slow raster uniformity, (a) and (c) are from the data, (b) is simulated.

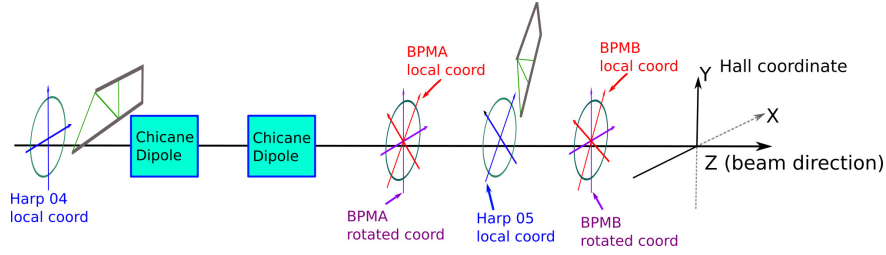


Figure 8: Coordinate systems used in this paper

127 to avoid the non-uniformity. The pattern of the spread beam was relatively
 128 uniform after this adjustment during the experiment, as shown in Fig.7(c).

129 3. Data analysis

130 3.1. Coordinate system

131 The relationship of coordinate systems used in this paper is shown in Fig.
 132 8.

133 The Hall coordinate is the global coordinate system in the hall, with the
 134 origin of the NH_3 target. The positions in the hall coordinate are identified as
 135 capital X and Y .

136 The origin of each local coordinate system is the surveyed location for each
 137 device. The angular components of survey data decide the orientation of each

local coordinate system. The positions in each local coordinate system are identified as lowercase x and y . If multi-coordinates are related in the equation, a superscript is used to indicate the local coordinate system: $x^{bpm/harp}$ and $y^{bpm/harp}$. The rotation between the BPMA local coordinate and the Hall coordinate is about 45° , while it is about 57° between the BPMB local coordinate and the Hall coordinate.

The harp scan data analysis was taken in the harp local coordinate. The calculated positions from two harps were transferred to the BPM local coordinate in order to calibrate the BPMs.

The BPM calibration was taken in the BPM local coordinate. In the straight through setting without the target magnet field, the positions calculated from the BPMs were transferred to the Hall coordinate in order to transport to the target location. For the settings with a transverse magnetic field, the input terms of the transport functions are the positions in the BPM rotated coordinate, which has the same origin with the BPM local coordinate but with the same directions with the Hall coordinate. The positions in the BPM rotated coordinate are identified as x^{rot} and y^{rot} .

3.2. Harp scans for measuring absolute beam position

An example of a harp scan result is shown in Fig.9.

There are three groups of recorded data for each harp scan, which are “index”, “position”, and “signal”. The index is related to the moving steps of the fork during the scan. Each step of the index increases by 0.008-0.07 mm depending on the speed of the motor driver [5]. The position is the wire location for each index. The testing results show a good linear relation between the position and the index as shown in Fig.9(a), because the motor speed is uniform. The line is the fitted result with $pos = a * index + b$. According to this linear relation, interpolation or extrapolation can be applied when a few data points are missing, in some cases. The strength of signal vs. position is plotted in Fig.9(b). Each peak represents the location when one of the three wires passed through the beam.

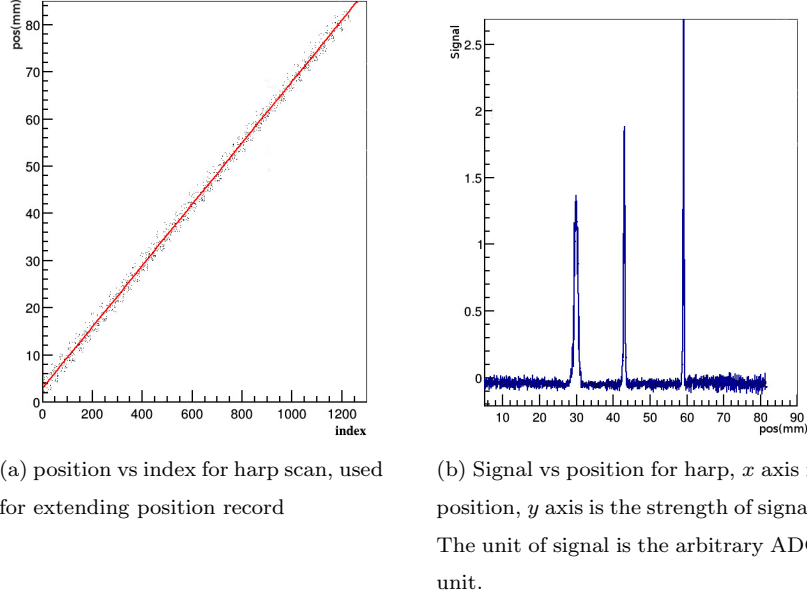


Figure 9: 1H05A harp scan data

168 The positions measured by the two harps were used for calibrating the beam
 169 positions in the two BPMs. When the chicane magnets were on, beam did not
 170 pass straight through from the first harp to the second harp. BPM calibrations
 171 using two harps were only possible when the chicane magnets were off, i.e. in the
 172 straight-through settings. Since the BPM was calibrated in the local coordinate
 173 system, the calibration constants were independent from the settings of other
 174 instruments. To make sure that the calibration constants for the BPMs were
 175 still valid during the non-straight-through settings, the settings for the BPM
 176 receiver were kept the same as in the straight-through settings during production
 177 running.

178 The scan data from the harps was not reliable when the current of CW beam
 179 (100% duty factor) was lower than 100 nA due to the low signal-to-noise ratio.
 180 The harp scans were taken in pulsed mode at a current of a few μA , while the
 181 BPMs were used for production data taking in CW mode at a beam current
 182 of 50-100 nA. For a BPM calibration run, a harp scan was done first in pulsed

mode, then a DAQ run was taken immediately to record the ADC value in CW mode without changing the beam position. The harp scan was then taken again in the pulsed mode to double check the beam position. The harp scan data was discarded and the scan was taken again if the beam position changed.

3.3. BPM data analysis and calibration

The traditional diff/sum method to calculate the beam position has the non-linearity effect in the position far away from the center of the beam pipe [8]. It is necessary to correct the equation of diff/sum since we have a slow raster. From the method of image [9, 10], the signal from each antenna excited by the beam can be calculated by:

$$\phi_i = \phi_0 I \frac{R^2 - \rho^2}{R^2 + \rho^2 - 2R\rho \cos(\theta_i - \theta_0)}, \quad (4)$$

where ϕ_i is the signal received in the antenna, and i is x_+ , x_- , y_+ and y_- , respectively, ϕ_0 is a constant related to the geometry of the BPM-chamber and the output resistance, I is the beam current, R is the radius of the BPM vacuum chamber, ρ is the radial position of the beam, and $\theta_i - \theta_0$ is the angle difference between the antenna and the beam in the polar coordinate .

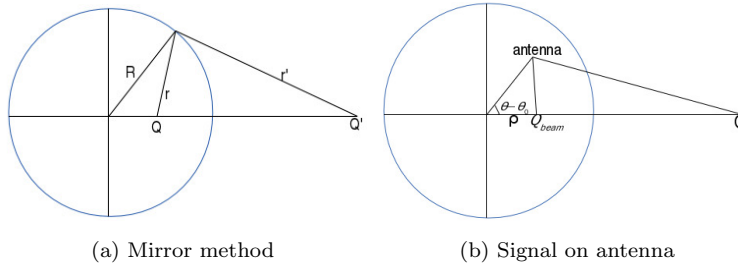


Figure 10: Signal for each antenna of BPM

The four antennas in the BPM chamber are used to determine the beam positions x and y in the BPM; x_+ and x_- for the x position, and y_+ and y_- for the y position. In order to extract the beam position information, and eliminate

201 the dependence on the beam current in equation (4), the difference-over-sum
 202 method is used as follows:

$$x_d = \frac{\phi_{x+} - \phi_{x-}}{\phi_{x+} + \phi_{x-}}, \quad (5)$$

$$y_d = \frac{\phi_{y+} - \phi_{y-}}{\phi_{y+} + \phi_{y-}}. \quad (6)$$

203 Substituting equation (4) into equation (5) and equation (6), they can be rewrit-
 204 ten as follows:

$$x_d = \frac{\phi_{x+} - \phi_{x-}}{\phi_{x+} + \phi_{x-}} = \frac{2}{R} \frac{\rho \cos(\theta - \theta_0)}{1 + \frac{\rho^2}{R^2}} = \frac{2}{R} \frac{x}{1 + \frac{x^2 + y^2}{R^2}}, \quad (7)$$

$$y_d = \frac{2}{R} \frac{y}{1 + \frac{x^2 + y^2}{R^2}}, \quad (8)$$

205 where $\rho^2 = x^2 + y^2$. When $x^2 + y^2 \ll R^2$, equations (7) and (8) can be simplified
 206 as:

$$\begin{aligned} x &= \frac{R}{2} x_d = \frac{R}{2} \frac{\phi_{x+} - \phi_{x-}}{\phi_{x+} + \phi_{x-}}, \\ y &= \frac{R}{2} y_d = \frac{R}{2} \frac{\phi_{y+} - \phi_{y-}}{\phi_{y+} + \phi_{y-}}. \end{aligned} \quad (9)$$

207 Equation (9) can be used in the simple case when the beam is near the center of
 208 the beam pipe. When the beam is far from the center, equation (9) is no longer
 209 valid. For the g2p experiment, the beam was rastered to have a diameter of
 210 about 2 cm at the target. Combining equation (7) with (8) the beam position
 211 can be calculated as:

$$\begin{aligned} x &= R x_d \left(\frac{1}{x_d^2 + y_d^2} - \frac{1}{\sqrt{x_d^2 + y_d^2}} \sqrt{\frac{1}{x_d^2 + y_d^2} - 1} \right), \\ y &= R y_d \left(\frac{1}{x_d^2 + y_d^2} - \frac{1}{\sqrt{x_d^2 + y_d^2}} \sqrt{\frac{1}{x_d^2 + y_d^2} - 1} \right). \end{aligned} \quad (10)$$

212 To verify this corrected equation, a simulation was performed. First, a set of
 213 position data was generated (Fig.11(a)), and the designed radius for the BPM

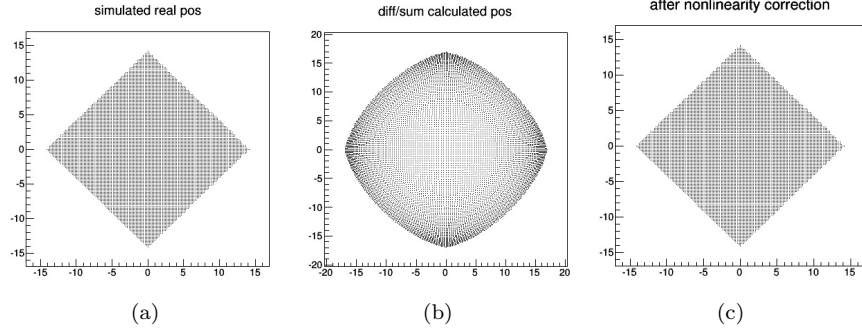


Figure 11: Comparing the calculated results using equation (9) and (10) with simulated position. (a) Simulated position; (b) The calculated result with equation (9), (c) The calculated result with equation (10).

214 chamber was used for R . Using equation (4) to get the signal for each an-
 215 tenna, and setting ϕ_0 and I to be equal to 1, equations (9) and (10) were used
 216 to calculate the beam position. The results are shown in Fig.11(b) and 11(c),
 217 respectively. In this way the method using equation (10) can correct the non-
 218 linearity effect caused by equation (9). Assuming the slow raster spreads the
 219 beam uniformly by changing the slow raster magnet current, the slow raster
 220 magnet current can be used to check this non-linearity. The slow raster mag-
 221 net current can be converted to the displaced position, more details about the
 222 conversion will be discussed in chapter 3.5. Fig. 12 shows the linearity of the
 223 corrected equation with the position converted from the slow raster, compared
 224 with position calculated from the diff/sum equation. In order to avoid the delay
 225 time caused by the BPM receiver, the waveform of the slow raster x-magnet was
 226 set to 20 Hz sinusoidal for this study. The slow raster y-magnet and the fast
 227 raster were kept off. Since the BPM has a 45° rotation with the Hall coordinate,
 228 the beam was sweeping in the diagonal direction in the BPM local coordinate,
 229 which has the largest non-linearity effect from the Fig. 11(c). The result shows
 230 that the corrected equation has a better linearity than the diff/sum one. Better
 231 solution may use a corrected algorithm during the benchmark test of the hard-
 232 ware [11]. The handling of the BPM information only used for the center beam

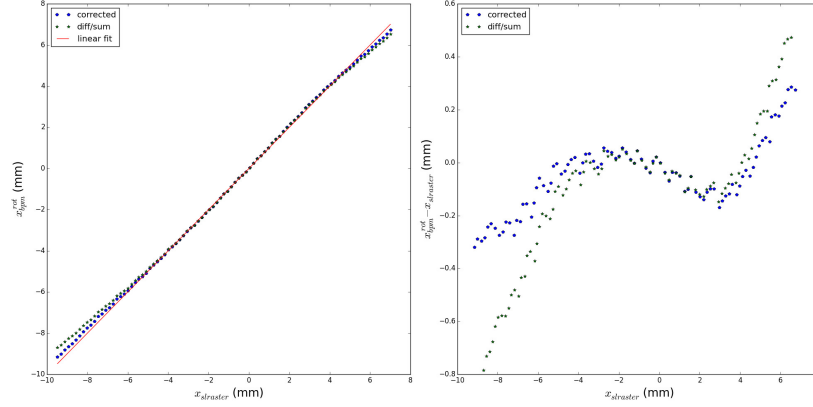


Figure 12: Linearity of the corrected equation compared with the diff/sum equation. The blue pentagon markers are calculated from the corrected equation, while the green star markers are calculated from the diff/sum equation. The x axis x_{raster} is the position transferred from the raster magnet current. The y axis in the left side is the position calculated from the BPM in the rotated coordinate system. The y axis in the right side is the absolute difference between the position calculated from BPM and the position transferred from the raster magnet current.

position (discussed in chapter 3.5) also reduced this non-linearity effect.

The final information recorded in the data-stream was designed to have a linear response with the raw signal in the 50-100nA current range. The ϕ_i in equation (7) can be rewritten as:

$$\phi_i = a_i(A_i - A_{i_ped} + b_i), \quad (11)$$

where A_i and A_{i_ped} are the recorded ADC value and pedestal value, and a_i and b_i are the slope and intercept of the relationship between ϕ_i and $A_i - A_{i_ped}$.

Equation (9) can be rewritten as:

$$x_d = \frac{(A_{x+} - A_{x+-ped} + b_{x+}) - h_x(A_{x-} - A_{x--ped} + b_{x-})}{(A_{x+} - A_{x+-ped} + b_{x+}) + h_x(A_{x-} - A_{x--ped} + b_{x-})}, \quad (12)$$

$$y_d = \frac{(A_{y+} - A_{y+-ped} + b_{y+}) - h_y(A_{y-} - A_{y--ped} + b_{y-})}{(A_{y+} - A_{y+-ped} + b_{y+}) + h_y(A_{y-} - A_{y--ped} + b_{y-})}, \quad (13)$$

where $h_x = a_{x-}/a_{x+}$, and is related to the ratio of the signals for the x_+ and x_- antennas and the gain settings of the two channels. Similarly, $h_y = a_{y-}/a_{y+}$.

Combining the equation (11) and (4), the calibration constant b_i was obtained by taking the linear fit between the ADC values of BPM and the beam current with a group of runs with the same beam position but different values of beam current: $I \propto (A_i - A_{i_ped} + b_i)$. Figure 13 shows the $A_i - A_{i_ped}$ versus

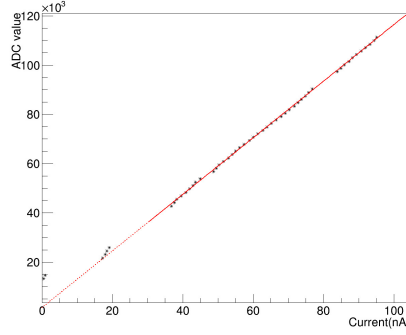


Figure 13: ADC value of BPM raw signal ($A - A_{ped}$) V.S. current

the beam current. It can be seen that the ADC values were linear with beam current in the considering current range of 50-100 nA. The intercept from the linear fit of Fig.13 is the value b_i .

Combining a group of the harp scan data with a group of the BPM data, the position determined from the harps was then used to calibrate the x and y position calculated in equation (10) using the following equations:

$$\begin{aligned} x_{harp}^{bpm} &= c_0 + c_1 x + c_2 y, \\ y_{harp}^{bpm} &= c'_0 + c'_1 x + c'_2 y, \end{aligned} \quad (14)$$

where x_{harp}^{bpm} , y_{harp}^{bpm} were projected from x_{harp} and y_{harp} in equation 2, c_0, c_1, c_2 and c'_0, c'_1, c'_2 are the calibration constants, which from a fit to the bpm data with the harp scan data, as an example shown in Fig. 14. The asterisks in Fig. 14 represent the beam positions x_{harp}^{bpm} and y_{harp}^{bpm} in the local coordinate of the BPM calculated with the harp scan data, and the dots at the center of the asterisks are the BPM data from the ADC after calibration. Figure 14(b)

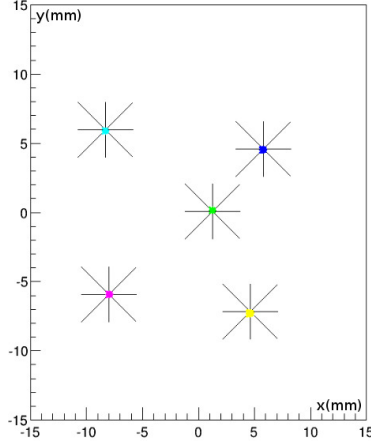


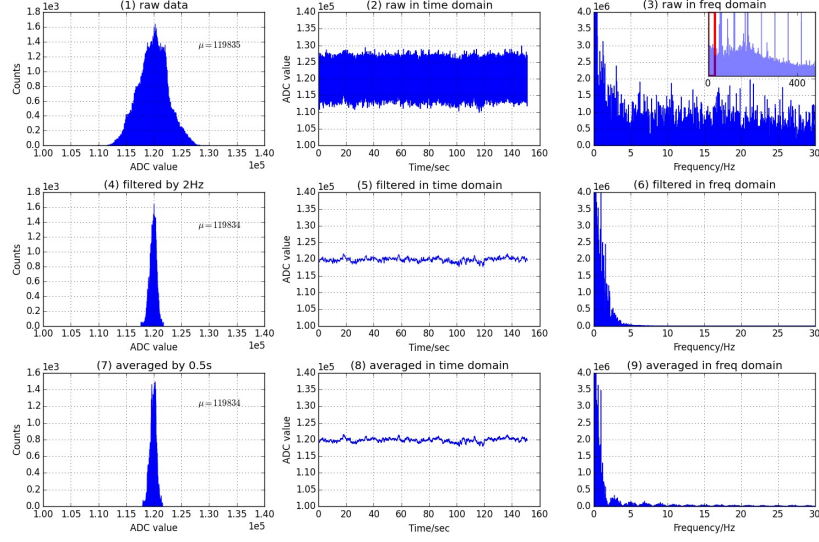
Figure 14: Harp scan data combined with DAQ data, the asterisk is the harp scan data, while the dot is the DAQ data after applying the calibration constants.

is the beam distribution recorded in the ADC of the BPM with the slow raster
on after applying the calibration constants.

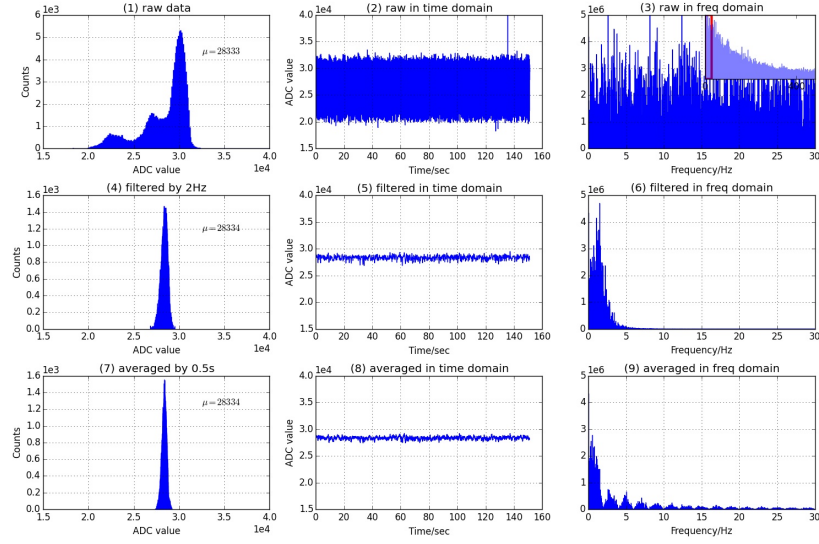
In order to reduce the noise and improve the resolution during data analysis,
a software filter was applied. Since the 18 bit ADC was triggered by the helicity
signal with a fixed frequency, it could be regarded as a sampling ADC. Fig.15
shows the signal dealt with a 2 Hz low pass filter. By sacrificing the high
frequency signal, higher resolution was gotten. The bottom 3 plots in Fig. 15
(a,b) are the averaged signal for comparing with the filtered signal. The average
procedure also sacrificed the high frequency part of the signal, which lead to the
same result as the filter. The filter also erases the beam displacement caused
by the rasters, which is necessary to extract the position of the beam center.

3.4. Beam position reconstruction at the target

It is easy to transport the position from the BPMs to the target by using a
linear transportation method for the straight through setting. For the settings
with a transverse magnetic field at the target, the linear transportation method
can not be used since the beam is bent near the target. A simulation package
was constructed to simulate the behavior of the beam. Polynomial curve fittings



(a) Normal run with beam



(b) Pedestal run without beam

Figure 15: Software filter applied to BPM signal. (a) is the signal with beam, (b) is the pedestal signal without beam. (1,2,3) in (a,b) are the raw signal without applying the filter, (4,5,6) are applied a 2Hz finite-impulse-response filter with 4th order. (7,8,9) are averaged with 0.5 s. (1,4,7) are the signal's 1-D histogram, (2,5,8) are the signal in time domain, (3,6,9) are in frequency domain. Note all of the plots in (a) is for a single signal, same as in (b).

275 were used for simulated data to generate the transport functions in order to
 276 transport the beam from the two BPMs to the target (Fig.16).

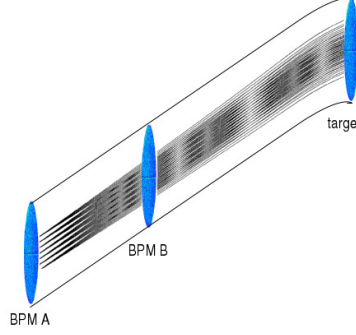


Figure 16: Transporting beam position from BPM to target with transverse target magnet field

276
 277 A target magnet field map [12] was generated from the TOSCA model. To
 278 test the accuracy of the TOSCA model, the target magnet field was measured
 279 before the experiment [13, 14]. The generated field map was used in the simula-
 280 tion. An event generator generated thousands of electrons with different initial
 281 positions and angles, with the energy of the electrons set to the same values as
 282 in the experiment. The Runge-Kutta method² with 0.02 mm step length was
 283 used to generate the trajectories from BPM A to the target by using the field
 284 map. The positions at BPM A, BPM B and the position and angle at the target
 285 were extracted from the simulated trajectory.

286 Data extracted from the simulation was used as input to a fitting program
 287 that determined the best-fit polynomial. In total, 24 different fits were taken for
 288 4 different target positions and 6 configurations with different target magnetic
 289 field and beam energy settings. The validity of the transport functions was
 290 explored in the simulation using a new set of random trajectories generated in
 291 the same manner as those used in the fitting. The deviation between the fitted
 292 transport function and the simulation was less than 0.1%.

²http://en.wikipedia.org/wiki/Runge-Kutta_methods

293 The transport functions were only used to transport the beam center position
 294 from the two BPMs to the target by applying the 2 Hz filter, which filtered out
 295 the fast raster and slow raster motion to keep only the beam center position.
 296 The transported position were expressed as X_{center} and Y_{center} .

297 3.5. Determining the beam position event-by-event

298 The readout of the magnet current for the two rasters was connected to
 299 a series of ADCs. Two scintillator planes in the HRS form a DAQ trigger.
 300 This pulse signal triggered the ADC to record the raster magnet current for
 301 each event. The information from the rasters and the BPMs was combined
 302 to provide the beam position event-by-event. The position at the target was
 303 determined as:

$$\begin{aligned} X &= X_{center} + X_{fstraster} + X_{slraster}, \\ Y &= Y_{center} + Y_{fstraster} + Y_{slraster}, \end{aligned} \quad (15)$$

304 where $X_{fstraster}$, $Y_{fstraster}$ and $X_{slraster}$, $Y_{slraster}$ were the position displaced
 305 by the fast raster and slow raster, respectively, which were converted from the
 306 current values of the two raster magnets. The calibration of the conversion
 307 factors between the magnet current of the rasters and the displaced position
 308 will be discussed in the next subsection. An example of reconstructed beam
 309 position is shown in Fig. 17.

310 3.5.1. Conversion factor for the slow raster

311 Two methods were used to calibrate the conversion factor for the slow raster.
 312 The first method used the calibrated BPM information, i.e., comparing the
 313 raster magnet current with the beam shape shown in the ADC of the BPMs.
 314 Several calibrations were taken during different run periods at a beam current of
 315 100nA using different values of the raster magnet current, as shown in Fig.18(a).

316

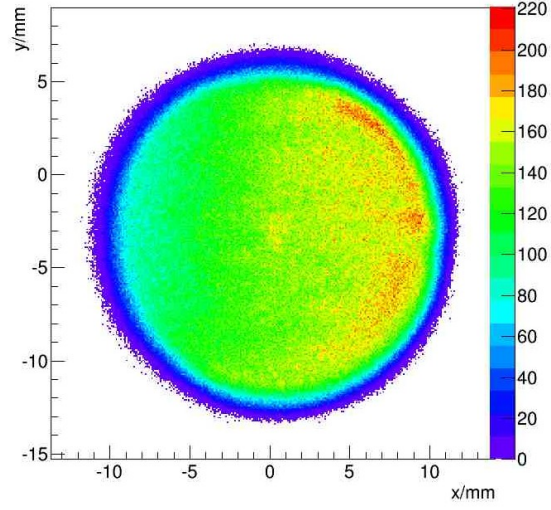


Figure 17: Reconstructed beam position at the target

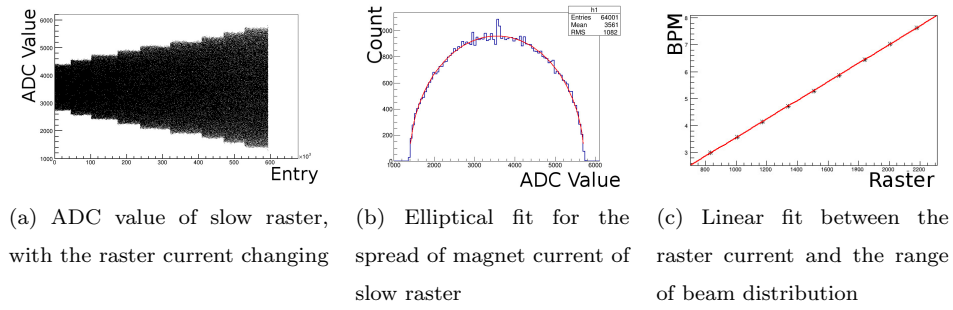


Figure 18: Converting the raster current to beam position shift

317 The range of the beam distribution at the target was calculated from the
 318 ranges at the two BPMs without applying the filter, using the transport func-
 319 tions fitted previously. The range of the beam distribution at the two BPMs
 320 and the amplitude of the raster current was calculated from an elliptical fit,
 321 an example is shown in Fig.18(b). Figure 18(c) shows a linear fit between the
 322 raster current and the range of the beam distribution at the target. The x axis
 323 in Fig.18(c) is the magnet current of the raster, and the y axis is the range of
 324 the beam distribution obtained from the BPMs.

325 The second method for calibrating the conversion factor used a target called
 “carbon hole” as shown in Fig.19(a).

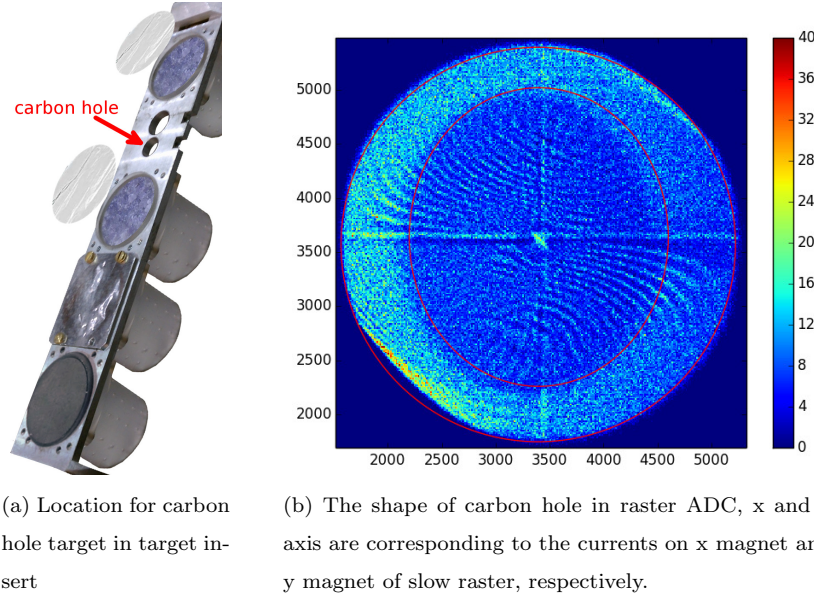


Figure 19: Carbon hole method to calibrate raster

326
 327 Scattered electrons were used as the trigger for recording the raster magnet
 328 current. Since the density of the target frame was much higher than that of the
 329 “hole”, which was submerged in liquid helium, the density of events triggered
 330 from the target frame was much higher than that of the hole itself. Recorded
 331 values reveal a hole shape as shown in Fig.19(b). The size of the carbon hole

332 was surveyed before the experiment, and a fit program was used to extract the
 333 radius of the recorded hole shape for that raster current. The conversion factor
 334 F was then calculated as the ratio of the size of the carbon hole S_{hole} and the
 335 radius of the hole shape R_{hole} in the ADC:

$$F = \frac{S_{hole}}{2 * R_{hole}}. \quad (16)$$

336 3.5.2. Conversion factor for the fast raster

337 The conversion for the fast raster was the same as for the slow raster. The
 338 low pass filter for the BPM was set to a higher value than the frequency of the
 339 fast raster to see the beam shape at the BPM formed by the fast raster. For a
 340 higher frequency filter, a larger beam current was needed to get a clear pattern.
 341 The beam current chosen for calibrating the fast raster was near 300 nA, which
 342 was the safety limit for the target. The beam shape formed by the fast raster
 is shown in Fig.20.

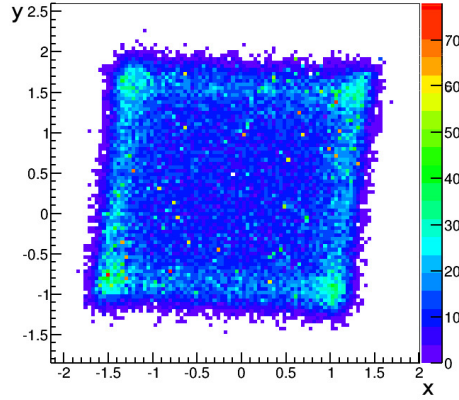


Figure 20: Beam shape formed by the fast raster at the BPM A location, the unit is millimeter

343

344 4. Uncertainty

345 The uncertainty of the final beam position at the target for each event con-
 346 tains several contributions:

- 347 • The first part comes from the uncertainty of the calibration constant. It
348 includes the BPM resolution for the DAQ runs used for the calibration,
349 the uncertainty of the harp data corresponding to each calibration, and
350 the survey uncertainties for the BPMs and harps. It contributes about 0.7
351 mm for the uncertainty of the position and 0.7 mrad for the uncertainty
352 of the angle.
- 353 • The uncertainty on the pedestal is the largest uncertainty for the beam
354 position measurement, contributing about 0.7~1.5 mm to the uncertainty
355 of the position and 0.7~1.5 mrad to the uncertainty of the angle.
- 356 • The uncertainties from the BPM survey need to be included, since the
357 production data and the calibration data were taken at different beamline
358 settings when the equipment was moved. They contribute 0.5 mm to the
359 uncertainty of the position.
- 360 • The uncertainty from the magnetic field map of the target was considered
361 for the settings with the target magnet field.
- 362 • The uncertainties due to the size conversion of the rasters were also in-
363 cluded.

364 The position uncertainty was magnified by a factor of 5 at the target because of
365 the short distance between the two BPMs. For example, in the straight through
366 setting, if the uncertainty at BPM A is 0.2 mm, and at BPM B is 0.27 mm,
367 the uncertainty at the target is 1.1 mm for position and 1.3 mrad for angle.
368 The uncertainty for the position at the target was around 1~2 mm, while the
369 uncertainty for the angle was 1~2 mrad.

370 5. Summary

371 JLab g2p experiment used a transversely polarized NH_3 target for the first
372 time in Hall A. It put a limit of below 100 nA on the electron beam current and
373 required a slow raster to spread beam to a large area. Two chicane magnets were

374 used to compensate the strong transverse magnetic field. Beam-line equipment,
 375 including the BPMs, harps and associated readout system, were upgraded to
 376 allow precision measurements of the beam position at low current (50-100 nA).
 377 A software filter was used to reduce noise in the BPMs. A corrected equation
 378 was used to compensate the non-linearity caused by the diff/sum equation. The
 379 harp data and the linear fit between the bpm signal and the beam current were
 380 used to extract the calibration constant of the BPM. To account for the strong
 381 target magnetic field effect, transport functions were generated to transport the
 382 beam position from the BPMs to the target. The beam position in the x-y plane
 383 and the angle at the target location are extracted event-by-event by combining
 384 information from the BPMs and the signals from the rasters. The performance
 385 of the new devices (BPMs, harps and slow rasters) were presented along with
 386 an analysis of systematic uncertainties.

387 **Acknowledgments**

388 This work was supported by DOE contract DE-AC05-84ER40150 under
 389 which the Southeastern Universities Research Association (SURA) operates the
 390 Thomas Jefferson National Accelerator Facility, and by the National Natural
 391 Science Foundation of China (11135002, 11275083), the Natural Science Foun-
 392 dation of Anhui Education Committee (KJ2012B179).

393 **Reference**

- 394 [1] A. Camsonne, J. P. Chen, D. Crabb and K. Slifer, spokesperson, JLab
 395 E08-027 (g2p) experiment. 1
- 396 [2] D. G. Crabb, W. Meyer, Solid polarized targets for nuclear and particle
 397 physics experiments, Annu. Rev. Nucl. Part. Sci. 47 (1997) 67–109. 1
- 398 [3] R. Michaels, Precision Integrating HAPPEX ADC, JLab Technical report
 399 (unpublished).

400 URL http://hallaweb.jlab.org/parity/prex/adc18/prex_adc18_
401 [spec.ps](#) 2.1

402 [4] J. Musson, Functional Description of Algorithms Used in Digital Receivers,
403 JLab Technical report No. JLAB-TN-14-028. 2.1

404 [5] C. Yan and et al., Superharp - A wire scanner with absolute position read-
405 out for beam energy measurement at CEBAF, Nuclear Instruments and
406 Methods in Physics Research A 365 (1995) 261–267. 2.2, 3.2

407 [6] J. Pierce, J. Maxwell, T. Badman, J. Brock, C. Carlin, D. Crabb, D. Day,
408 C. Keith, N. Kvaltine, D. Meekins, J. Mulholland, J. Shields, K. Slifer,
409 Dynamically polarized target for the and experiments at jefferson lab,
410 Nuclear Instruments and Methods in Physics Research Section A: Acceler-
411 ators, Spectrometers, Detectors and Associated Equipment 738 (0) (2014)
412 54 – 60. doi:<http://dx.doi.org/10.1016/j.nima.2013.12.016>.
413 URL [http://www.sciencedirect.com/science/article/pii/](http://www.sciencedirect.com/science/article/pii/S0168900213016999)
414 [S0168900213016999](#) 2.3

415 [7] C. Yan, Hall C Polarized Target Raster System Upgrade, JLab Technical
416 report (unpublished).
417 URL https://www.jlab.org/Hall-C/talks/01_06_05/yan.pdf 2.3

418 [8] W. . Barry, A general analysis of thin wire pickups for high frequency beam
419 position monitors, Nuclear Instruments and Methods in Physics Research
420 A 301 (1991) 407–416. 3.3

421 [9] C.R.Carman, J. L. Pellegrin, The beam positions of the spear storage ring,
422 SLAC-PUB-1227. 3.3

423 [10] P.Poit, Evaluation and correction of nonlinear effects in fnpl beam position
424 monitors, FNPL Technical report No.Beams-doc-1894-v1.
425 URL [http://beamdocs.fnal.gov/AD-public/DocDB/ShowDocument?](http://beamdocs.fnal.gov/AD-public/DocDB/ShowDocument?docid=1894)
426 [docid=1894](#) 3.3

- 427 [11] M. Spata, T. Allison, K. Cole, J. Musson, J. Yan, Evaluation and Cor-
428 rection of the Non-Linear Distortion of CEBAF Beam Position Monitors,
429 Poster, Proceedings of IPAC 2011, San Sebastian, Spain.
430 URL [http://accelconf.web.cern.ch/accelconf/ipac2011/papers/](http://accelconf.web.cern.ch/accelconf/ipac2011/papers/tupc172.pdf)
431 [tupc172.pdf](http://accelconf.web.cern.ch/accelconf/ipac2011/papers/tupc172.pdf) 3.3
- 432 [12] R. Wines, private communication. 3.4
- 433 [13] J. Liu, Magnetic field mapping on a translation table, JLab Technical
434 report, E08-027 Collaboration (unpublished).
435 URL [http://hallaweb.jlab.org/experiment/g2p/collaborators/](http://hallaweb.jlab.org/experiment/g2p/collaborators/jie/2011_10_05_fieldmap_report/Target_Field_Map_Report.pdf)
436 [jie/2011_10_05_fieldmap_report/Target_Field_Map_Report.pdf](http://hallaweb.jlab.org/experiment/g2p/collaborators/jie/2011_10_05_fieldmap_report/Target_Field_Map_Report.pdf) 3.4
- 437 [14] C. Gu, Target field mapping and uncertainty estimation, JLab Technical
438 report, E08-027 Collaboration (unpublished).
439 URL [https://hallaweb.jlab.org/experiment/g2p/collaborators/](https://hallaweb.jlab.org/experiment/g2p/collaborators/chao/technotes/Chao_TechNote_TargetField.pdf)
440 [chao/technotes/Chao_TechNote_TargetField.pdf](https://hallaweb.jlab.org/experiment/g2p/collaborators/chao/technotes/Chao_TechNote_TargetField.pdf) 3.4